



Microstructural features and metastable phase formation in a high-strength aluminum alloy fabricated using additive manufacturing

Andrew D. Iams^{a,*}, Jordan S. Weaver^{b,2}, Brandon M. Lane^{b,3}, Lucille A. Giannuzzi^{c,4}, Feng Yi^{d,5}, Darby L. LaPlant^e, John H. Martin^{e,6}, Fan Zhang^{d,*,7}

^a Materials Science and Engineering Division, Material Measurement Laboratory, National Institute of Standards and Technology, Gaithersburg, MD 20899, USA

^b Intelligent System Divisions, Engineering Laboratory, National Institute of Standards and Technology, Gaithersburg, MD 20899, USA

^c L.A. Giannuzzi & Associates LLC, Fort Myers, FL 33913, USA

^d Materials Measurement Science Division, Material Measurement Laboratory, National Institute of Standards and Technology, Gaithersburg, MD 20899, USA

^e HRL Laboratories LLC, Malibu, CA 90265, USA

ARTICLE INFO

Keywords:

Aluminum alloys
Microstructure
Analytical microscopy
Quasicrystal
Additive manufacturing
Powder bed fusion

ABSTRACT

Additive manufacturing (AM) has opened new pathways for producing high-strength aluminum alloy components. However, optimizing their mechanical performance require a detailed understanding of microstructural evolution. In this study, a multi-length-scale microstructural and computational analysis was conducted on a commercially available, precipitation-hardenable aluminum alloy (AA7A77) in the as-fabricated condition. A distinct bimodal microstructure influenced by the solidification process was observed, with fine equiaxed grains near the melt-pool boundaries and coarse elongated grains within the center of the melt pool. Two key metastable phases were identified: the cuboidal $L1_2$ Al_3Zr phase within fine grains and the icosahedral $Mg_{32}(Al, Zn, Cu)_{49}$ quasicrystal located within coarse grains and along grain boundaries. Computational simulations provided insight into the formation of the quasicrystals, where a secondary phase was predicted to form at the termination of solidification which is favorable to quasicrystal formation. Nanoindentation demonstrated a hardness comparable to peak-aged AA7075, which leads to the possibility of further improvement through a precipitation-hardening heat treatment. This work provides new insights into the microstructural characteristics of high-strength AM aluminum alloys and presents a novel pathway for leveraging quasicrystals for enhanced mechanical performance.

1. Introduction

Additive manufacturing (AM) of aluminum alloys has transformative potential for various industries, such as aerospace and automotive, because of its ability to create lightweight components with complex geometries, improve material efficiency and sustainability, and shorten engineering and production cycles. Despite these advantages, the AM process has its challenges for aluminum alloys, because AM's high temperatures and rapid cooling rates can result in microstructural

heterogeneities that deviate from traditional wrought counterparts, which can negatively impact mechanical performance [1–4].

For instance, the most commonly used high-strength aluminum alloys (2xxx, 6xxx, and 7xxx series) are often produced using direct chill casting, with the liquid metal temperatures ranging between 690 °C to 725 °C and solidification cooling rates typically between 0.4 °C/s to 10 °C/s [5,6]. These alloys subsequently undergo controlled thermo-mechanical processing steps to refine the microstructure and material properties to meet specific performance criteria.

* Correspondence to: 100 Bureau Drive, Gaithersburg, MD 20899-8520, USA.

E-mail addresses: andrew.iams@nist.gov (A.D. Iams), fan.zhang@nist.gov (F. Zhang).

¹ 0000-0003-1176-8093

² 0000-0003-4857-5164

³ 0000-0001-5153-1678

⁴ 0000-0002-1353-3303

⁵ 0000-0002-8269-3685

⁶ 0000-0002-8238-6845

⁷ 0000-0003-1248-0278

In contrast, the fabrication of aluminum alloys using laser-powder bed fusion, can experience liquid metal temperatures beyond 3000 °C and solidification cooling rates exceeding 10^6 °C/s [7]. Such highly nonequilibrium processing diverge significantly from traditional fabrication practices, introducing unique challenges such as the vaporization of alloying elements [8–14], the formation of metastable phases [15], and the development of metallurgical defects [13,16–23].

Solidification cracking [24], also known as hot tearing [6,25], represents a prevalent type of metallurgical defect that high-strength AM aluminum alloys are especially susceptible to. This defect occurs near the end of the solidification process when the remaining liquid metal fails to compensate for the volumetric contraction and tensile stresses that arise during the liquid-to-solid transition. Such cracks compromise the structural integrity of the AM parts [1–4], making them less desirable for high-performance applications that AM materials are targeted for.

Using inoculant particles for grain refinement is a common mitigation strategy to minimize solidification cracking in high-strength aluminum alloys. This approach has previously been implemented in casting [6] and welding [24], and more recently found applications in AM [11,13,20,26–36]. Introducing inoculant particles can promote the formation of equiaxed grains, enhance the microstructural homogeneity, improve the flow and feeding of liquid metal during solidification, and reduce localized stress concentrations. These improvements decrease the susceptibility of AM materials to solidification cracking [24].

In the case of the 7000 series aluminum alloys, often considered to be among the strongest aluminum alloys, grain refinement in AM can be achieved through alloying the powders with elements such as Zr, Sc, and Ti. During solidification, tri-aluminide intermetallics such as Al_3Zr , Al_3Sc [37], and Al_3Ti are among the first phases to crystallize from the molten alloy, serving as heterogeneous nucleation sites for subsequent aluminum grain growth. This leads to a fine and equiaxed grain structure. Notably, aluminum alloy (AA)7A77 [38], one of the earliest commercial high-strength AM aluminum alloys, utilizes this Zr-based grain refinement mechanism to minimize solidification cracking [13].

While the use of inoculants has become integral to the development and commercialization of high-strength AM aluminum alloys, there remains a significant knowledge gap concerning the microstructure of these materials in their as-fabricated state, particularly concerning their grain structures and secondary phases. Given that these high-strength AM aluminum alloys are typically precipitation-hardenable, understanding the microstructure in the as-fabricated condition is critical because this initial microstructure serves as the starting point for subsequent heat treatments, thereby influencing the ultimate mechanical properties of the material.

In this study, we used AA7A77 as the subject to examine the as-fabricated microstructure across multiple length scales. Our analysis revealed that the AM process introduces a variety of metastable phases within the microstructure. Specifically, we identified two distinct grain morphologies: fine, equiaxed grains containing Al_3Zr phases and coarser grains characterized by a previously unreported icosahedral quasicrystal. To elucidate the mechanisms impacting the formation of these secondary phases, we combined analytical structural characterization techniques with computational thermodynamic simulations. Additionally, mechanical testing indicated the as-fabricated AA7A77 material exhibits hardness levels comparable to those of peak-aged AA7075. Our findings offer insights into the design and application of high-strength AM aluminum alloys and contribute to optimizing the AM processing and subsequent post-processing steps. Our results could also contribute to the development of high-performance AM aluminum alloys with novel alloy compositions and improved mechanical properties.

2. Material and methods

A series of cubic structures, each measuring approximately 20 mm in

each dimension, were fabricated from AA7A77 powder (HRL Laboratories LLC, Malibu, USA) using a Renishaw[#] 500Q laser powder bed fusion (LPBF) additive manufacturing system (Renishaw Inc., Wotton-under-Edge UK) and utilizing a reduced build volume. The system had an integrated ytterbium fiber laser, with a central emission wavelength between 1068 nm to 1082 nm. During the deposition process, the laser was operated as a modulated continuous laser, with a power of 250 W, scanning speed of 1333 mm/s, to create individual layers with a thickness of 30 μm . The D4 σ laser spot size was estimated to be 80 μm . The hatch spacing between laser passes was set at 80 μm . Throughout the manufacturing process, high-purity argon gas was introduced into the build chamber at a flow rate of 180 m³/h to serve as an inert shielding environment. All samples were produced utilizing the processing parameters outlined above. The AA7A77 powder utilized to create the cube structures exhibited a D₅₀ particle size range from 35 μm to 45 μm . Autogenous single pass laser scans were carried out on cubes from the initial build in a separate EOS M290 LPBF system (EOS GmbH, Krailling DE) using two sets of laser parameters; one equivalent to the parameters used to fabricate the cube structures, and another using a power of 350 W, scanning speed of 750 mm/s, and an estimated spot size of 100 μm . The larger spot size (100 μm) was achieved by moving the sample above the recoating plane by 2.65 mm. The purpose of exploring two single pass laser parameters was to better understand the impact on solidification cooling rates. All single pass microstructures presented within this manuscript correspond to the parameters used to fabricate the cubic structures.

The compositional analysis of the as-fabricated material was conducted using industry-standard techniques at a certified testing laboratory. The results of this analysis are presented in Table 1. Utilizing these measured compositions, computational thermodynamic simulations, assuming equilibrium conditions, were carried out to predict phase fractions as a function of temperature. The CALPHAD (CALCulation of PHase Diagrams) method was employed, utilizing Thermo-Calc Software version 2022b [39,40] and the TCAL3 database [41] (Thermo-Calc Software, Solna SE). Additionally, a Scheil-Gulliver model (referred to as Scheil hereafter) within the Thermo-Calc software was used to simulate the phases formed during the solidification from liquid to solid. The Scheil model assumed negligible diffusion within the solid phases, diffusion within the liquid phase is infinitely fast, and local equilibrium is maintained at the solid-liquid interface [42,43]. Compared to computational thermodynamic predictions under equilibrium assumptions, the Scheil model has been shown to better predict experimentally observed phases under the rapid solidification conditions of AM [44]. This improved predictive capability is attributed to the rapid convective mixing occurring within the molten pool, which aligns with the fundamental assumption built into the Scheil model of infinitely fast diffusion within the liquid.

Metallographic specimens were extracted from the cubic structures using a metallographic diamond saw with cooling. These samples were mounted in a thermosetting epoxy resin prior to surface preparation. The surface was ground using silicon carbide (SiC) grinding paper with a grit size conforming to P4000 ISO standards. This was followed by a three-stage polishing process: initial polishing employed a 3 μm diamond slurry, a subsequent stage used a 1 μm diamond slurry, and final polish used a colloidal silica solution having a particle size of 0.06 μm .

For microstructural characterization, Scanning Electron Microscopy (SEM) analyses were performed using a JEOL 7100 SEM system (JEOL Ltd., Tokyo JP) equipped with a Symmetry S2 detector (Oxford Instruments, Abingdon UK). Electron Backscatter Diffraction (EBSD)

[#] Certain commercial products, commercial and open source software are identified in this paper to specify the materials used and the procedures employed. In no case does such identification imply endorsement or recommendation by the National Institute of Standards and Technology, nor does it indicate that the products are necessarily the best available for the purpose.

Table 1

Measured composition reported as mass fraction for the bulk as-fabricated AA7A77 material (%). Values were provided by an external laboratory and uncertainties were not provided.

Condition	H	O	Mg	Al	Si	Cr	Fe	Cu	Zn	Zr
As-fabricated	0.003	0.077	2.94	Bal.	0.08	0.01	0.10	1.61	5.96	1.79

measurements were taken at an operating voltage of 20 kV and a current of 3.5 nA. A step size of 0.1 μm was employed for these measurements, and data were acquired and analyzed using the AZtec software package (Oxford Instruments, Abingdon, UK). No interpolation and/or modification through filtering or cleaning was used for the EBSD data.

routines Samples for Transmission Electron Microscopy (TEM) were prepared through a multi-step process. First, the cube structures were sectioned to a nominal thickness of approximately 2 mm. Subsequently, both sides of these sections were ground using SiC grinding paper with an ISO P800 grit size, reducing the thickness to form 300 μm foils. Circular specimens, 3 mm in diameter, were punched out from these foils. Twin-jet electro-polishing (Fischione Instruments, Export USA) was then employed to achieve electron transparency. The electrolyte solution for this electro-polishing consisted of a 400 mL methanol to 100 mL nitric acid (HNO_3) ratio, and was maintained at a temperature ranging from -31°C to -22°C .

For imaging, a Titan analytical TEM (Thermo Fisher Scientific, Waltham USA) equipped with a Gatan (AMETEK, Inc., Berwyn USA) OneView IS CMOS camera was used, operating at an accelerating voltage of 300 kV for conventional TEM analysis. Scanning TEM (STEM) images were acquired using a Talos F200X TEM (Thermo Fisher Scientific, Waltham USA) at an accelerating voltage of 200 kV, employing high-angle annular dark field (HAADF) imaging. Elemental compositional mapping was conducted using a Super-X Detection system (Thermo Fisher Scientific, Waltham USA). Data were analyzed using the Cliff-Lorimer quantification method [45] within the ESPRIT software package (Bruker Nano GmbH, Berlin DE).

A G200 nanoindenter (KLA Corporation, Milpitas USA) with a diamond Berkovich tip was used to measure the modulus and hardness using the Oliver-Pharr method [46]. The area function was calibrated on a quartz reference sample using a continuous stiffness module (CSM) and constant strain rate (CSR) test method. This area function was also used for rapid test results and found to produce comparable hardness values on the quartz reference sample (see [Supplemental Material](#)). Utilizing the Rapid Test Method, loads and unloads to a single depth at a much faster rate compared to the CSM-CSR Test Method. Both the CSM-CSR and Rapid Test Methods were used on as-built AA7A77 samples and yielded similar hardness results. Hardness values reported in the main text are from Rapid Tests with a displacement range of 220 nm to 280 nm. An indent spacing to depth ratio > 10 was maintained with a typical ratio > 20 for arrays of indents.

3. Results

3.1. Solidification cooling rates

Understanding the solidification cooling rates can provide valuable insights to microstructural formation. As a result, in-situ thermography and as-deposited solidification structures were analyzed. In the as-fabricated AA7A77, distinct dendritic solidification features were observed within the grain structures, which permitted the approximation the solidification cooling rates. Cooling rates were determined from two sets of processing parameters, as detailed in [Table 2](#). By employing an established empirical relationship [47]:

$$\lambda = 4.128 \times 10^{14} \times R^{-3.195} \quad (1)$$

where λ (nm) is primary dendrite arm spacing (PDAS) and cooling rate is R ($^\circ\text{C/s}$), PDAS were linked to the cooling rates. The resulting estimated

Table 2

Processing parameters used to measure the primary dendrite arm spacing.

Power (W)	Speed (mm/s)	Estimated Spot Size (μm)	Measured PDAS (nm)	Estimated Cooling Rate ($^\circ\text{C/s}$)
250	1333	80	205 ± 71	6.5×10^6 to 6.6×10^7
350	750	100	364 ± 85	1.4×10^6 to 6.3×10^6

cooling rates for as-fabricated AA7A77 ranged from 1.4×10^6 $^\circ\text{C/s}$ to 6.6×10^7 $^\circ\text{C/s}$. Our observations confirm that utilizing lower laser power and faster travel speed results in smaller PDAS and more rapid cooling rates. This is consistent with the expectations for LPBF [48], where slower cooling rates typically allow dendrites more time to grow, leading to increased spacing between the primary arms. Furthermore, our PDAS-derived cooling rates were corroborated by measurements obtained using in-situ thermography. These thermography measurements, detailed in the [supplementary data](#), indicated a melt pool surface cooling rate exceeding 1×10^6 $^\circ\text{C/s}$. More details about the thermography measurements of aluminum alloys will be reported separately. These observations confirm the cooling rates in AM aluminum alloys are substantially higher than those typically encountered in conventional aluminum alloy processing. The high rates of cooling are known to contribute to microstructures which deviate from traditional wrought aluminum products, including the formation of metastable phases [47].

3.2. Aluminum matrix within the AA7A77 microstructure

3.2.1. Aluminum grain size and morphology

The grain structure in the as-fabricated AA7A77 alloy displayed a mix of fine and coarse grains, as illustrated in [Fig. 1\(a\)](#). An area analysis of the grains was used to understand their size distribution and found that the coarse grains occupied a significant proportion of the total grain area despite their low number density. Specifically, our analysis of nearly 40 000 grains showed that 89 % of the grains had an equivalent circular diameter ranging from 200 nm to 1000 nm with a mean value plus/minus one standard deviation of ($509 \text{ nm} \pm 207 \text{ nm}$) accounting for 52 % of the total grain area. Conversely, the remaining 11 % of grains had diameters larger than 1000 nm with a mean value plus/minus one standard deviation of ($1427 \text{ nm} \pm 538 \text{ nm}$) and constituted 48 % of the area. In addition to grain size, the mean fitted ellipse aspect ratios plus/minus one standard deviation of the fine and coarse grains are (1.6 ± 0.5) and (1.9 ± 0.9), respectively. The fitted ellipse aspect ratios shows both grain types appeared near-equiaxed (a perfectly circular grain has a fitted ellipse aspect ratio values equal to 1.0) while the coarse grains appeared slightly more elongated.

While the bimodal grain structure is evident, the repeated thermal cycling from multiple laser passes can lead to an interpretation ambiguity in the formation and spatial distribution of these grain structures with respect to the melt pool. To better understand the AM process and its effects on the material, we conducted single-pass measurements on the as-fabricated AA7A77 samples. This simplified and better controlled approach isolates the laser-alloy interactions and provides direct insights into the resulting microstructure.

As illustrated in [Fig. 2\(a\)](#), the microstructure of the single-pass melt pool closely resembles that of the as-fabricated material, featuring both fine equiaxed grains and coarse elongated grains. The spatial

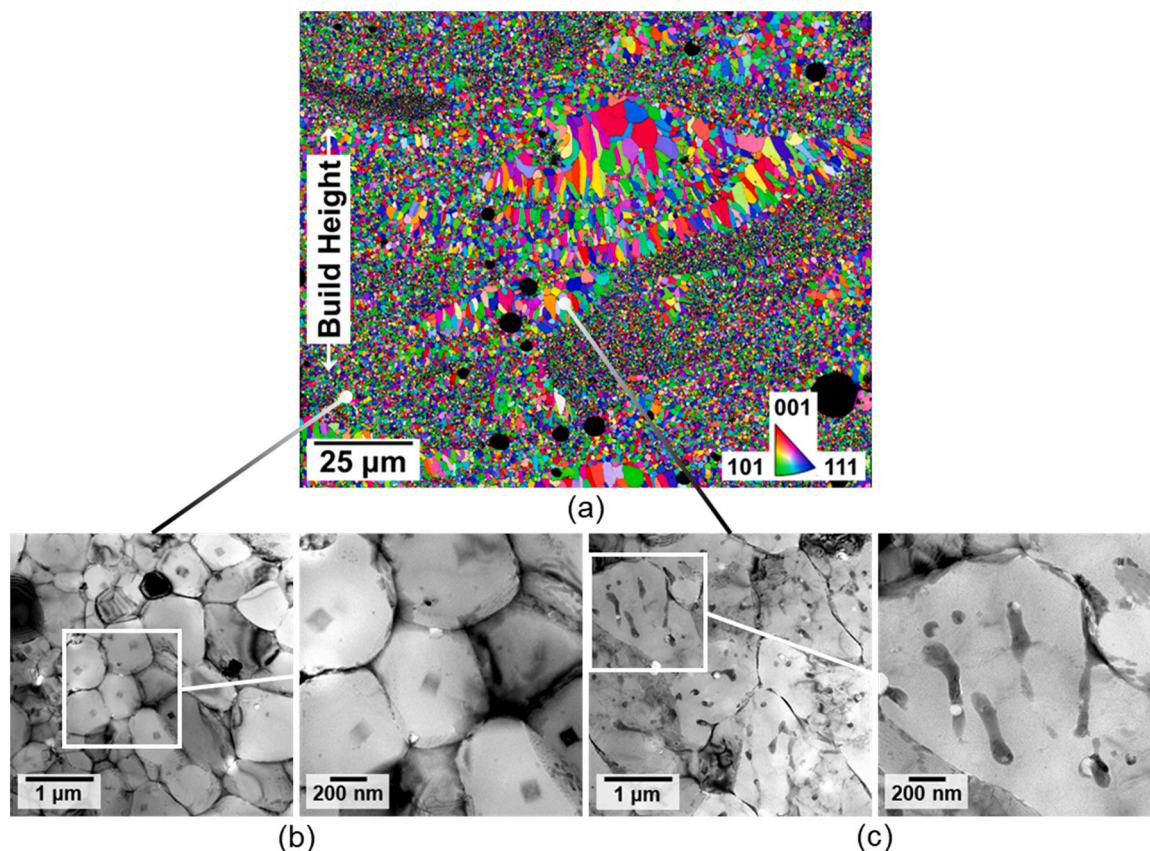


Fig. 1. (a) An SEM-EBSD IPF-Z colormap of the as-fabricated AA7A77 microstructure, (b)(c) showing bright field TEM images of (b) fine and (c) coarse grains regions.

organization of these different grain morphologies is distinct, with the fine equiaxed grains predominantly localized along the boundary of the melt pool and the coarse elongated grains situated in the central region of the melt pool. Such grain distribution patterns have previously been identified in high-strength aluminum fusion welds incorporating grain-refining alloying elements [24]. This microstructural behavior has also been observed within AM aluminum alloys that use grain-refining elements to mitigate the risks of solidification cracking [26–28,30,32,49]. Our single-pass experiment adds solid evidence to support this behavior.

3.2.2. Aluminum grain composition

In addition to size and morphology, the aluminum grain composition was also measured. STEM-EDS was used, and care was taken to isolate the composition of the aluminum matrix from the other secondary phases within the microstructure. The measured levels of Zr within the aluminum grains were significantly higher than the predicted solubility limits of Zr within the AA7A77, as listed in Table 3. Although, computational thermodynamic simulations under equilibrium and Scheil conditions predicted the maximum solubility of Zr within the AA7A77 matrix at a mass fraction of 0.17 (%), shown in Fig. 3(d), we see measured Zr levels 10–14 times higher. Similar elevated levels of Zr within the aluminum matrix have also been previously reported in high-strength aluminum alloys fabricated using AM [29]. These elevated levels of Zr have also been observed within Al-Zr binary alloys. Researchers have reported a solid solution binary alloy with a mass fraction composition of Al 96.6 (%) / Zr 3.4 (%) using rapid cooling rates near 1×10^7 °C/sec [50], while the Al-Zr phase diagram showed the maximum Zr mass fraction solubility near 0.1 (%). The high levels of Zr within the aluminum matrix can be attributed to the rapid cooling from liquid-to-solid [50–53].

More intriguing was the measured compositional variations

observed between the fine and coarse aluminum grains. The fine aluminum grains appeared depleted in Mg, Cu, Zn, and Zr compared to the coarse aluminum grains, as listed in Table 3. During the solidification of a molten pool, the areas around the fusion boundary will solidify first, analysis of the AA7A77 microstructure indicated this would be the fine grains. Results from Scheil simulations of the aluminum matrix and liquid compositions predicted increasing mass fractions of Mg, Cu, and Zn throughout the solidification process, with mass fractions lower early in the solidification (fine grain regions) and higher at the termination of solidification (coarse grain regions), shown in Fig. 3(c) and Fig. 3(e). The observed trends in the anticipated compositions of Mg, Cu, and Zn align well with experimental data. However, the mechanism(s) responsible for the variations in Zr remain unclear. One plausible explanation is that the formation of Al_3Zr within the fine grains might lead to the localized consumption of Zr in that specific region. Consequently, this phenomenon could contribute to the depletion of Zr in the fine grains compared to the coarse grains, where the precipitation of Al_3Zr is not observed. Nevertheless, further investigation is needed to elucidate these complex dynamics definitively.

3.2.3. Aluminum grain orientation

In both the as-fabricated and single-pass grain structures, a high frequency of grain misorientations near 60° was observed, as shown in Fig. 4(a). This high frequency significantly exceeded what would be expected from the theoretically random grain distribution (Mackenzie distribution in Fig. 4(a)). Interestingly, the prevalence of boundaries with misorientations near 60° was similar in both fine and coarse grain regions, with no apparent spatial variations within the microstructure. These grain boundaries are highlighted within the microstructure by red lines, shown in Fig. 4(b). To better understand these large misorientations, the pole figures for two grains with misorientations near

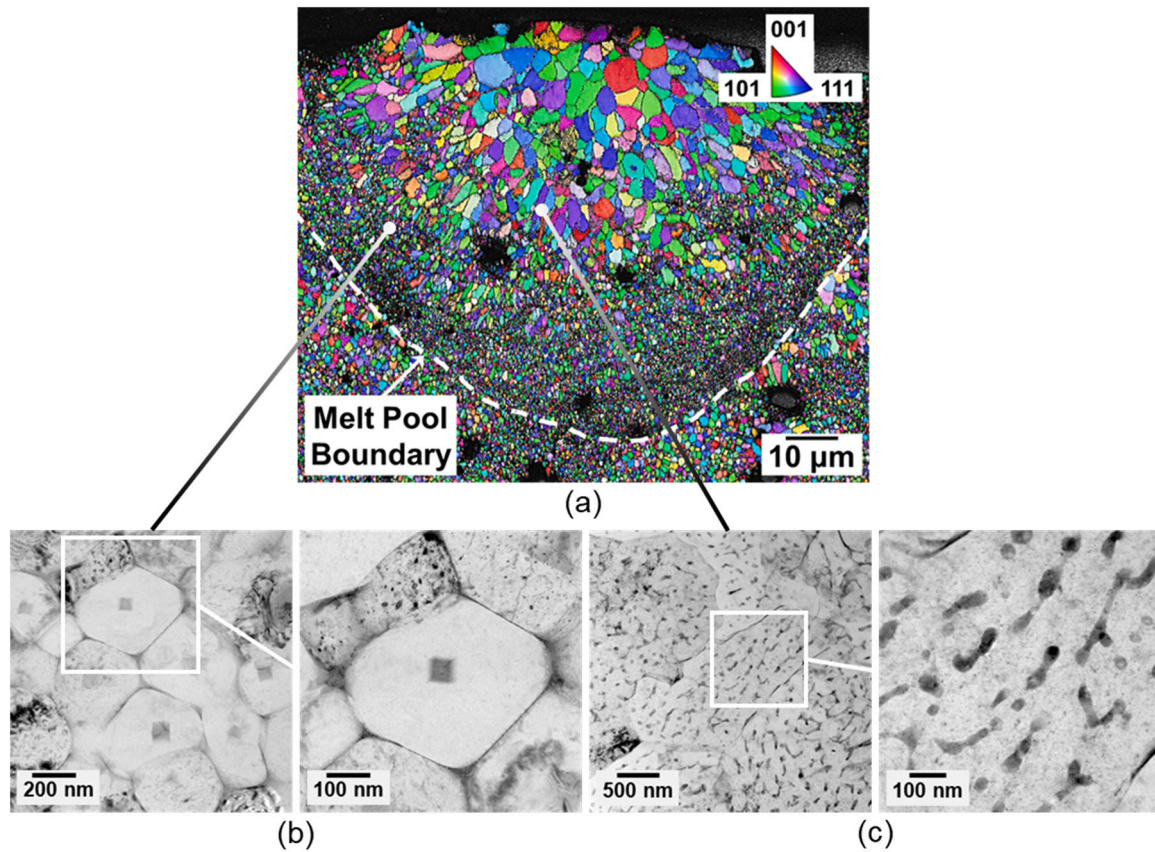


Fig. 2. (a) An SEM-EBSD IPF-Z colormap of an AA7A77 single pass microstructure, (b)(c) showing bright field TEM images of (b) fine grains along the melt pool boundary and (c) coarse grains within center of the pass.

Table 3

Measured and predicted mass fraction (%) composition of microstructural features within the as-fabricated AA7A77 material.

Phase	Mg	Al	Cu	Zn	Zr
Aluminum Matrix – Within Fine Grains	1.5 ± 0.1	89.8 ± 0.6	2.9 ± 0.3	4.1 ± 0.4	1.7 ± 0.4
Aluminum Matrix – Within Coarse Grains	2.1 ± 0.1	87.6 ± 0.5	3.6 ± 0.3	4.3 ± 0.2	2.4 ± 0.3
Al ₃ Zr	—	62.4 ± 3.6	—	—	37.6 ± 3.9
Icosahedral Phase – Within Coarse Grains	15.2 ± 0.5	29.5 ± 3.6	25.3 ± 2.4	30.0 ± 0.7	—
Icosahedral Phase – Along Grain Boundaries	16.3 ± 0.5	26.8 ± 2.2	24.6 ± 1.9	32.3 ± 2.0	—
Predicted T-Phase at 95 % fraction solid (temperature: 469°C)	21.4	27.9	16.1	34.6	—

Note: Average values and a single standard deviation are reported from the STEM-EDS measurements.

60° are presented in Fig. 4(c) and Fig. 4(d). From the pole figures, a twin relationship was observed, with the two grains sharing three common <110> directions and two <111> directions. Although twin boundaries are often thought of as straight coherent boundaries, incoherent wavy twin boundaries, similar to the boundary shown in Fig. 4(c), have been previously reported in aluminum alloys [54].

3.3. Secondary phases within the AA7A77 microstructure

The presence and morphology of secondary phases in AM aluminum alloys contribute to the overall material performance. Hence, their characterization is essential for understanding this manufacturing

process. Here, we conducted detailed analysis on the as-fabricated build and the single-pass samples to evaluate the secondary phases within the AA7A77 microstructure in detail. We found that the secondary phases predominantly reside in three distinct regions: near the center of the fine grains, distributed within coarse grains, and along grain boundaries.

Within the fine grains, we observed cuboidal secondary precipitates that are centrally located within each grain, as shown in Fig. 1(b) and Fig. 2(b). In contrast, the secondary phases within the coarse grains exhibited distinct, irregular morphologies distributed throughout the grains, as shown in Fig. 1(c) and Fig. 2(c). The location and morphologies of the secondary phases within the coarse grains indicated they originated in the interdendritic regions during the solidification process. Additionally, we observed secondary phase precipitates along the grain boundaries surrounding both the fine and coarse grains, as illustrated in Fig. 1 and Fig. 2. A comprehensive identification and description regarding the formation of these secondary phases will be detailed in the subsequent sections.

3.3.1. Secondary phase within fine grains: Al₃Zr

Compositional maps in Fig. 5 show that the cuboidal precipitates within the fine grains are enriched in Al and Zr. A fast Fourier transform of the HAADF STEM image reveals that these precipitates have a cubic L1₂ crystal structure and a mean lattice parameter plus/minus one standard deviation of (0.403 nm ± 0.001 nm), also shown in Fig. 5. Such compositional, morphological, and structural attributes are consistent with the Al₃Zr grain-refining precipitates. Additionally, the Al₃Zr precipitates have a cube-on-cube orientation relationship with the aluminum matrix, which has a nearly identical mean matrix lattice parameter plus/minus one standard deviation of (0.403 nm ± 0.003 nm). This close match in lattice parameters and orientation minimizes crystallographic disregistry, making the Al₃Zr precipitates

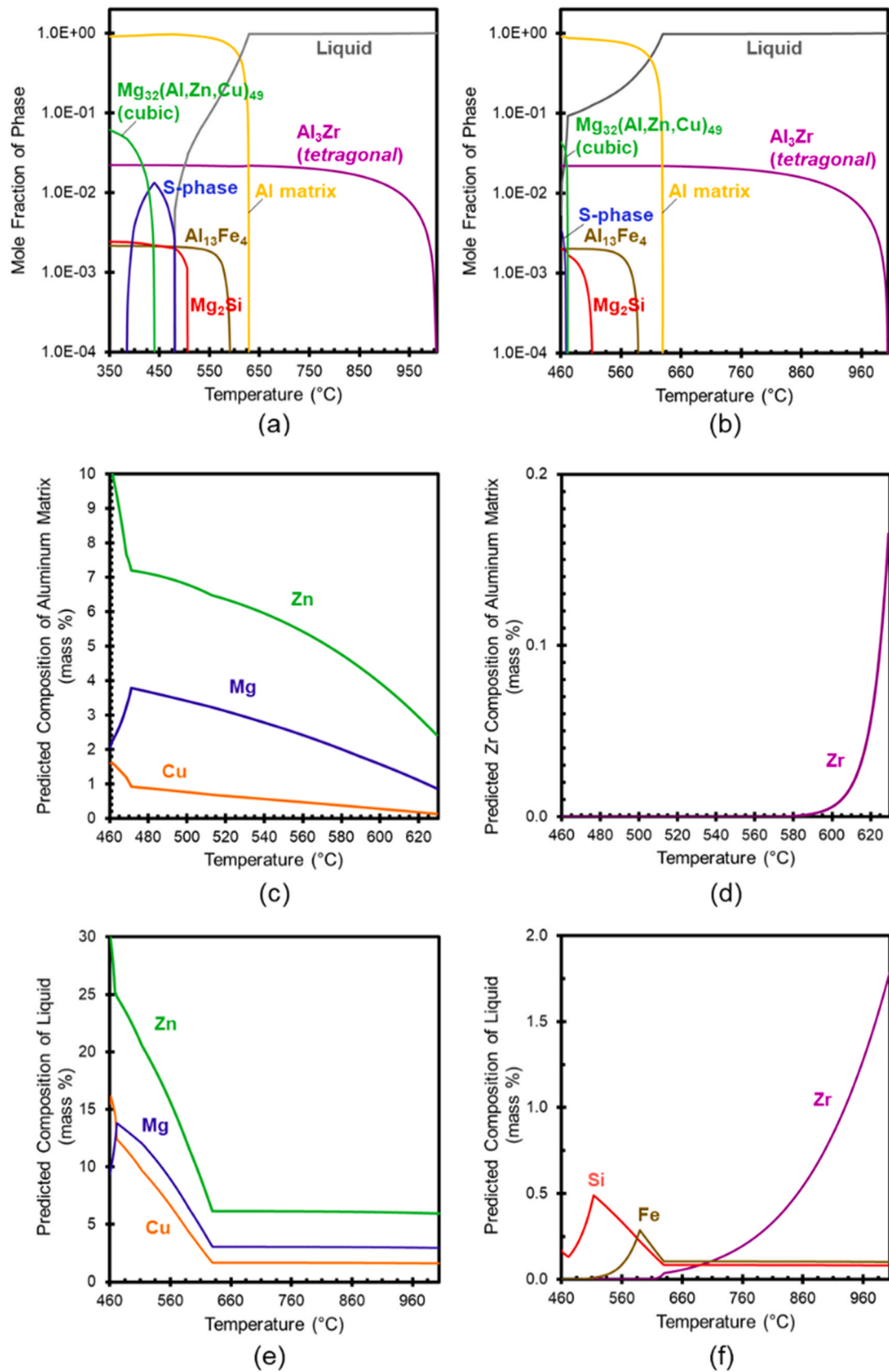


Fig. 3. Predicted phase fractions as a function of temperature using (a) equilibrium and (b) Scheil conditions for the AA7A77 material. Predicted (c)(d) aluminum matrix and (e)(f) liquid compositions as a function of temperature under Scheil conditions.

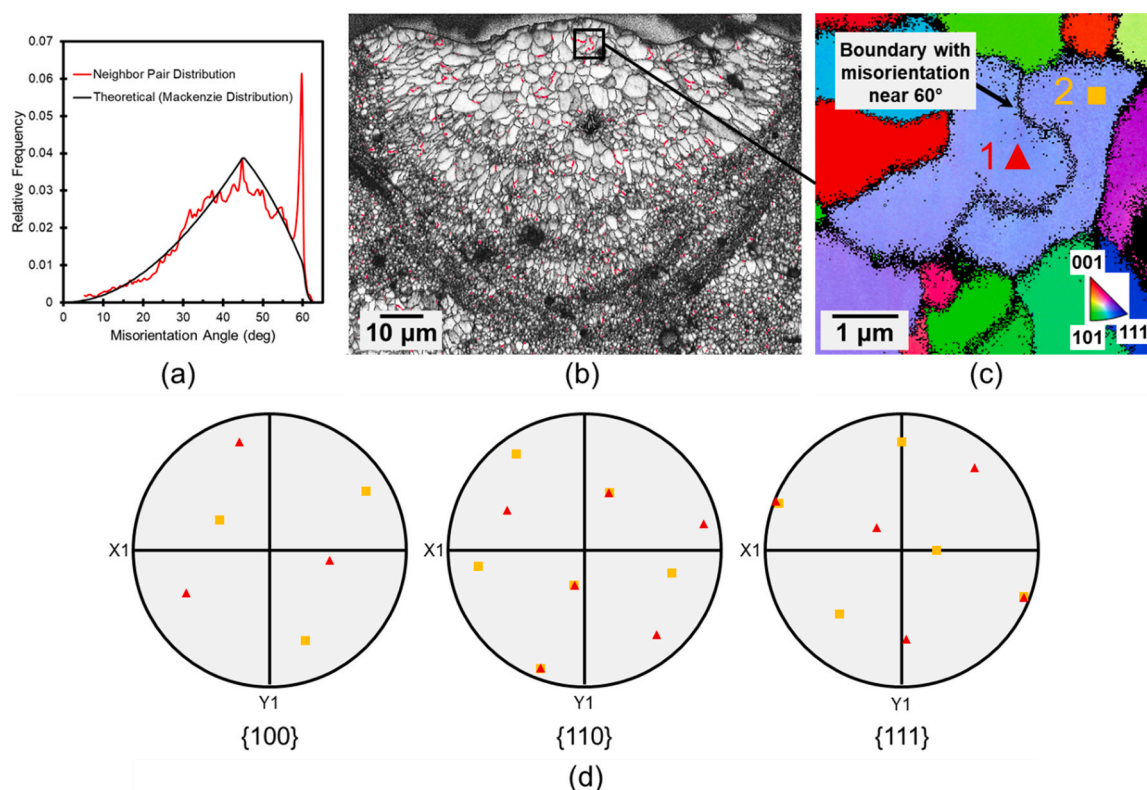


Fig. 4. (a) Nearest neighbor grain boundary misorientation histogram of the AA7A77 as-fabricated material compared to a theoretical random grain distribution. (b) Band contrast image of a single pass microstructure showing grain boundaries with misorientation near 60° highlighted in red. (c) IPF-Z colormap showing two aluminum grains, labeled 1 and 2, separated by a grain boundary with a misorientation near 60°. (d) Corresponding pole figures of grains labeled 1 and 2 shown within (c), which showed a twin boundary relationship.

effective sites for heterogeneous nucleation of the matrix grain [55]. The nominal size of the cuboidal precipitates was below 1 μm. This small size implies a high degree of undercooling, which correlates with a rapid nucleation rate and the formation of a large number of small grains, consistent with our observation of fine, equiaxed grains near the melt pool boundary.

We used computational thermodynamic simulations to understand the formation of Al₃Zr in the AA7A77. Both equilibrium and Scheil models predict that Al₃Zr with a tetragonal D0₂₃ structure will form first at a temperature of 1004 °C. This is followed by the aluminum matrix phase at 629 °C, as shown in Fig. 3. The agreement between our experimental findings and these simulations supports the design rationale for the AA7A77. Specifically, the addition of Zr beyond its solubility limit in AA7A77 (≈ 0.17 mass % at 630 °C) promotes the formation of Al₃Zr. These precipitates subsequently act as effective sites for the heterogeneous nucleation and growth of aluminum grains, thereby impacting the final microstructure of AA7A77.

While both equilibrium and Scheil simulations predicted the formation of Al₃Zr with a tetragonal D0₂₃ structure, they failed to capture the cubic L1₂ crystal structure that we observed. This discrepancy indicates the formation of the L1₂ structure originates from the nonequilibrium [56] process inherent to AM [28]. Our data on dendritic arm spacing and thermography indicate that AA7A77 experiences rapid cooling rates during AM processing, ranging from 1 × 10⁶ °C/s to 1 × 10⁷ °C/s. Such cooling rates promoted the formation of the metastable L1₂ phase, over the thermodynamically stable D0₂₃ state [53].

3.3.2. Secondary phases within coarse grains and along grain boundaries: icosahedral quasicrystal

In our as-fabricated AA7A77, we discovered a previously undocumented quasicrystalline secondary phase that is distributed extensively throughout the microstructure. This quasicrystalline phase is located

within the interdendritic regions of the coarse grains and along the grain boundaries, as shown in Fig. 6. Fast Fourier transforms of the high-resolution TEM images clearly reveals non-periodic spots and a 5-fold rotational symmetry, indicating the quasicrystalline nature of these phases. While twinning has been cited to cause similar observed rotational symmetries in reciprocal space [57], we emphasize that the atomic-scale imaging definitively verified that the 5-fold rotational symmetry originates from a single crystallite, as demonstrated in Fig. 7.

To confirm the quasicrystalline nature of this secondary phase, we performed TEM measurements on the same particle at three different zone axes. Fig. 8 shows the fast Fourier transforms of the high-resolution TEM images acquired by following the known tilt-angle relationships of common quasicrystal structures [58]. The data unambiguously demonstrate five-fold, three-fold, and two-fold symmetries. Leveraging the rotational and mirror symmetry within the fast Fourier transforms, we determined that the quasicrystals possess an icosahedral structure, characterized by a point group m $\bar{3}$ 5 [58]. Through indexing the two-fold pattern [59], we determined a mean quasilattice constant [60] plus/minus one standard deviation to be (0.516 nm ± 0.001 nm), as shown in Fig. 8(c).

Despite the quasicrystalline phases having different morphologies and being located in two distinct locations within the microstructure (specifically, the interdendritic regions within the coarse grains and along grain boundaries), they exhibit nearly identical composition and structure. Analysis of the compositional maps revealed these quasicrystalline phases are rich in Al, Cu, Mg, and Zn, as shown in Fig. 9. As listed in Table 3, quantitative analysis shows their compositional similarity.

Several studies have documented the presence of quasicrystalline phases within the microstructure of AM aluminum alloys [15,61–63]. However, these studies often lack comprehensive details on the

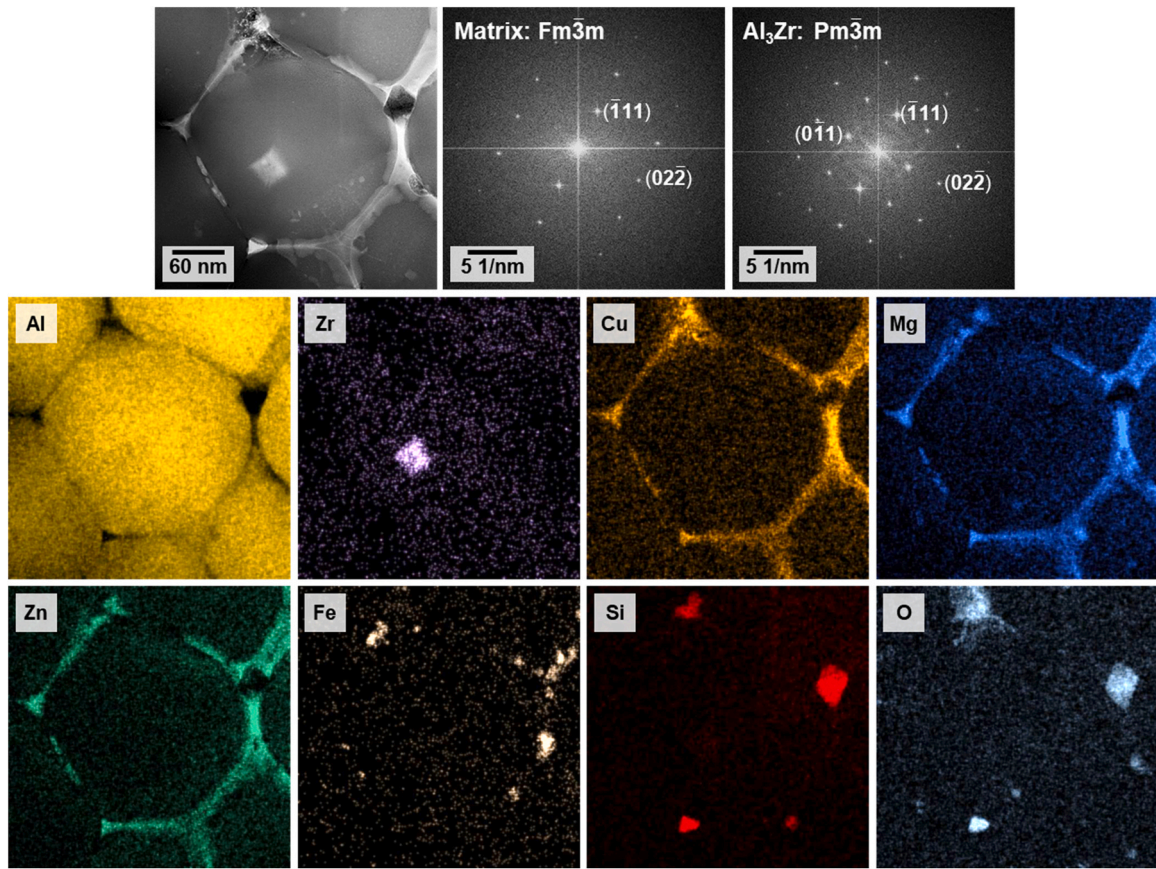


Fig. 5. A HAADF STEM image, corresponding fast Fourier transform of the aluminum matrix and Al_3Zr phases, and compositional maps of a characteristic fine aluminum grain within the as-fabricated AA7A77 microstructure.

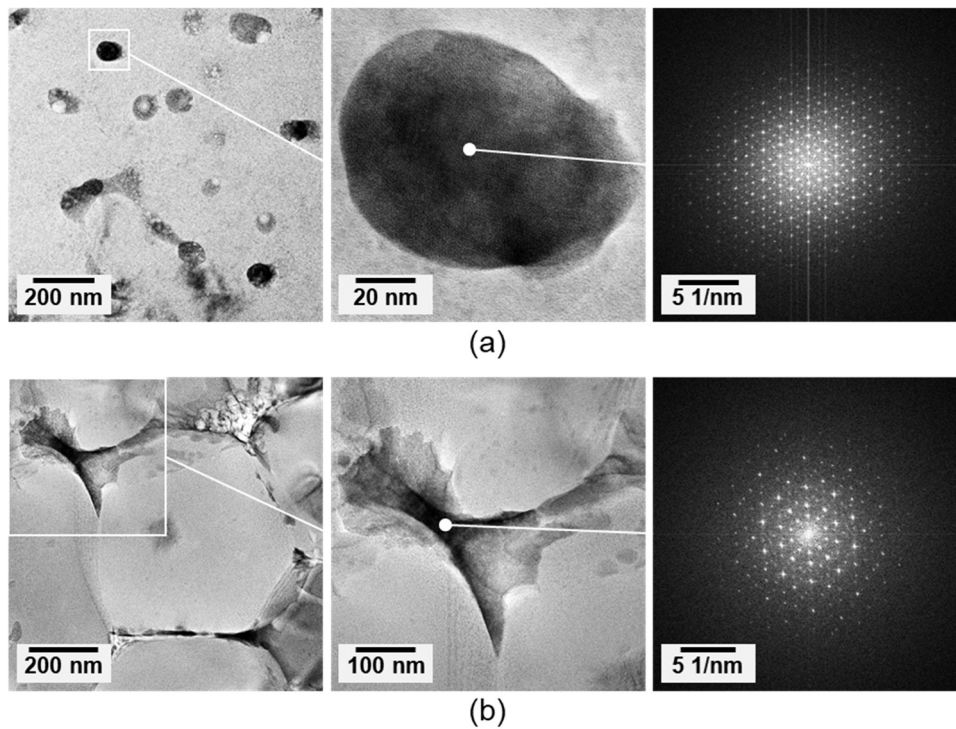


Fig. 6. TEM images and corresponding fast Fourier transforms of the secondary phases within the (a) columnar grains and (b) along grain boundaries within the as-fabricated AA7A77 microstructure. The FFTs showed non-periodic spots and exhibited a fivefold symmetry axis which indicated the secondary phases within the columnar grains and along grain boundaries were quasicrystalline.

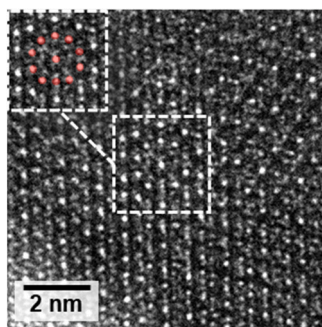


Fig. 7. A high-resolution TEM image along the fivefold symmetry zone axis of a characteristic quasicrystal secondary phase within the as-fabricated AA7A77 material.

compositional and structural characteristics, making comparative analysis difficult. Kairy et al., were the first to identify the formation of an icosahedral quasicrystalline phase within an AM aluminum alloy. Termed the ν -phase, this icosahedral structure was extensively observed throughout the microstructure and was rich in Al, Mg, Cu, and Zn, with a measured quasilattice constant of 0.49 nm [15]. In another study, Babu et al. reported the formation of an icosahedral quasicrystalline phase in an AM aluminum alloy, which they termed P-phase [63]. This phase was rich in Al, Zn, and Mg, and had a quasilattice constant of 0.529 nm.

Based on the chemical compositions and quasilattice constants, it seems unlikely that the quasicrystal within the AA7A77 microstructure is either ν - or P- phases. Instead, our observations appear to align closely with the $\text{Mg}_{32}(\text{Al}, \text{Zn}, \text{Cu})_{49}$ icosahedral quasicrystal, which has a quasilattice constant of 0.515 nm. Notably, this is the first reported instance of the formation of a $\text{Mg}_{32}(\text{Al}, \text{Zn}, \text{Cu})_{49}$ icosahedral quasicrystal in an AM context. Previously, its formation was achieved through traditional rapid solidification techniques, such as gun quenching and melt spinning [59].

To ensure comprehensiveness, we note that in addition to the Al_3Zr and the $\text{Mg}_{32}(\text{Al}, \text{Zn}, \text{Cu})_{49}$ icosahedral quasicrystal, evidence exists for three other secondary phases within the interdendritic regions of the coarse grains and along grain boundaries, as shown in Fig. 9. The presence of Mg_2Si was confirmed by identifying its crystal structure, lattice parameter, and composition. These details are provided in the [supplementary material](#). Computational thermodynamics support this experimental observation, suggesting the formation of Mg_2Si occurs near the end of the solidification process, shown in Fig. 3. This is consistent with its observed location in the interdendritic regions and at grain boundaries, where solidification is the last to occur. Additionally, we also identified secondary phases rich in Si-O and Al-Fe. However, we could not obtain data on their crystal structures and compositions due to their small size and low volume fractions.

3.4. Impact of microstructural features on the mechanical properties

The AA7A77 is engineered for high-strength applications. Hence, it is meaningful to evaluate the impact of our observed as-fabricated microstructure on the material's mechanical performance. The nano-indentation measurements on the as-fabricated material revealed a bulk hardness of $2.34 \text{ GPa} \pm 0.15 \text{ GPa}$ and an elastic modulus of $82.6 \text{ GPa} \pm 6.2 \text{ GPa}$, as detailed in Table 4. This bulk hardness value surpassed that of an as-fabricated 7xxx series aluminum alloy using Zr/Sc as grain refiners; in those alloys, the hardness values ranged from 1.83 GPa to 2.05 GPa under various processing conditions [64]. We note that in this Sc/Zr modified AA7075, quasicrystals were absent within the microstructure [64]. In our case, the hardness of the bulk AA7A77 material is nearly identical to that of the peak-aged wrought AA7075, which was reported at $2.41 \text{ GPa} \pm 0.08 \text{ GPa}$ [65]. We note the measured modulus is higher than anticipated for aluminum alloys, which is on the order of 72 GPa. Modulus values determined using nanoindentation within 10 % of reference values are frequently deemed acceptable. Considering the standard deviation on the mean values, our modulus met expectations for nanoindentation measurements and appeared consistent with previous reported values [64].

To gain a deeper understanding of how the microstructure and secondary phases contribute to these elevated hardness values, we conducted spatially resolved nanoindentation measurements on a single-pass AA7A77 specimen. This approach allows us to separate the contributions from the fine grain and coarse grain regions. Details of these measurements and illustrations of the results are shown in Fig. 10. Importantly, we observed that the spatial variations in hardness are strongly correlated with grain structures. The fine grain region, located near the melt pool boundary, have a hardness of $2.45 \text{ GPa} \pm 0.16 \text{ GPa}$. In contrast, the coarse grain regions, located in the center of the melt pool, have a hardness of $2.28 \text{ GPa} \pm 0.11 \text{ GPa}$.

The trend of elevated hardness in the fine grain regions compared to coarse grain regions is not unexpected. This behavior has been observed in other AM aluminum alloys [66,67] and may be readily attributed to the Hall-Petch effect. However, given the presence of the secondary phases, we undertook a comprehensive analysis to understand the relationship between microstructural features and the observed mechanical performance.

Two characteristic indentations, one within the coarse grain region and the other in the fine grain region, are shown in Fig. 10(a) and Fig. 10 (d), respectively. The indentation within the fine grain region contained multiple microstructural features, including at least 15 aluminum grains, several Al_3Zr precipitates, and secondary phases along the aluminum grain boundaries. As grain boundaries are known to impede dislocation motion, thus contributing to strengthening, the multitude of phase boundaries within the indentation likely contributed to the observed elevated hardness values.

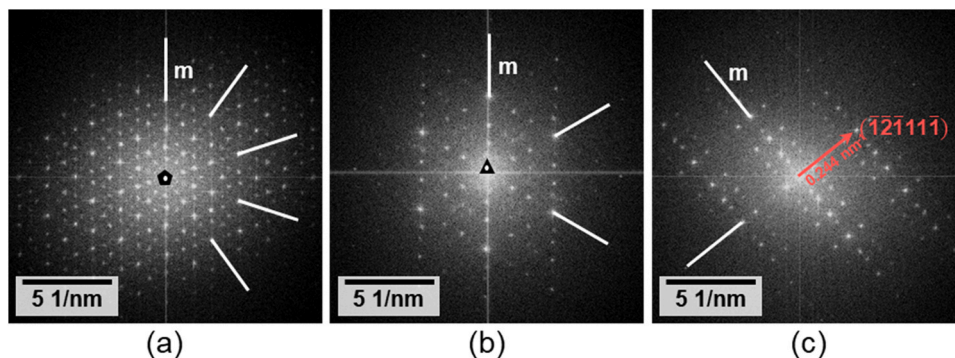


Fig. 8. The fast Fourier transformations of high-resolution TEM images collected from the same particle at three different zone axes, showing (a) five-fold, (b) three-fold, (c) two-fold symmetries. From the rotational symmetries and mirror planes exhibited in the patterns the quasicrystal structure was identified as icosahedral with a point group of $m\bar{3}5$. (c) The twofold pattern was used to determine the quasilattice constant which was found to be $0.516 \text{ nm} \pm 0.001 \text{ nm}$.

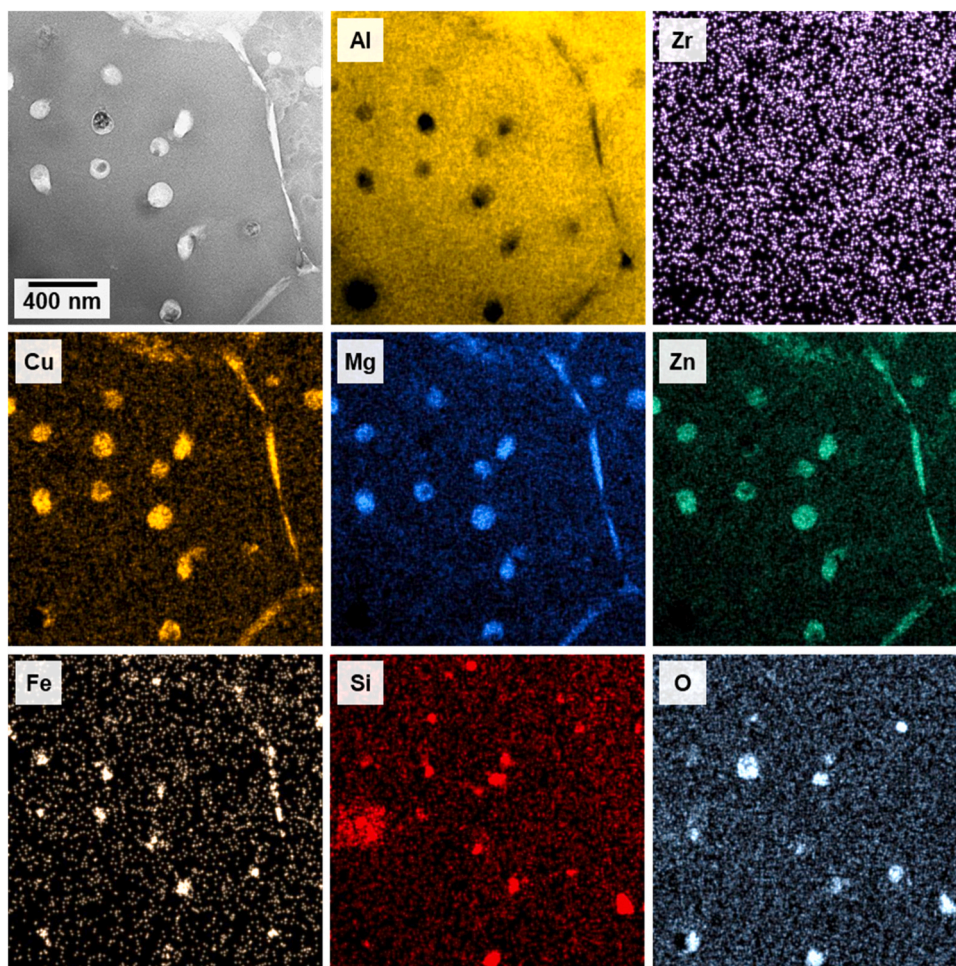


Fig. 9. A HAADF STEM image and corresponding compositional maps of a characteristic coarse aluminum grains within the as-fabricated AA7A77 microstructure.

Table 4

Nanoindentation data of the AA7A77 material.

Test Area	Elastic Modulus (GPa)	Hardness (GPa)
Bulk	82.6 ± 6.2	2.34 ± 0.15
Coarse Grain Region	82.1 ± 6.2	2.28 ± 0.11
Fine Grain Region	83.4 ± 6.1	2.45 ± 0.16

Note: Average values and a single standard deviation are reported from the nanoindentation measurements.

In contrast, the indentation in the coarse grain region was confined to a single aluminum grain. This grain contains widespread interdendritic secondary phases, predominantly composed of the $\text{Mg}_{32}(\text{Al}, \text{Zn}, \text{Cu})_{49}$ icosahedral quasicrystal. The aperiodic atomic packing of the quasicrystal lattice induces a crystallographic mismatch at the quasicrystal-matrix interface, which can result in local strain fields which contribute to dislocations [68]. Fig. 11 shows clear evidence of extensive dislocation networks around the interdendritic quasicrystals in the coarse grains. In addition to the quasicrystal itself, these complex dislocation networks can act as barriers for further dislocation motion, thereby strengthening the material and impacting the hardness results.

We also note that in the aluminum matrix in both the fine grain and coarse grain regions, we observed elevated levels of Zr, with Zr mass fractions at 1.7 ± 0.4 (%) and 2.4 ± 0.3 (%) for the fine grain region and coarse grain region, respectively. These concentrations are substantially higher than Zr equilibrium solubility in Al, primarily due to the solute trapping of Zr atoms within the aluminum matrix during rapid solidification, which extends the Zr solubility limit. Such high concentrations

of Zr in the matrix inevitably introduce lattice distortions, create strain fields near the Zr atoms, and serve to strengthen the material through the solid-solution strengthening. A comprehensive analysis will be required to delineate the contributions from a variety of strengthening mechanisms in the as-fabricated AA7A77.

4. Discussion

4.1. Aluminum grain structure

The mechanisms driving the formation of the observed bimodal microstructure remain unclear. However, the distinct spatial distribution of fine and coarse grains suggests that two separate grain growth mechanisms occur. Recent work using a 1D phase-field model, which incorporates factors such as solute diffusion, thermal diffusion, and solute trapping, aligns well with our empirical observations [69]. Specifically, in a hyperperitectic Al-1.2Zr system, the model suggests that initial solidification controlled by solute diffusion occurs near the melt-pool boundary, giving rise to equiaxed grains. Conversely, in the melt pool center, Al solidification controlled by thermal diffusion leads to the development of columnar grains. While these 1D model predictions are consistent with our observations, they do not fully capture the complexity of the grain growth mechanisms in AM. Given the inherent spatial complexities and directional dependencies within AM melt pools, high-dimensional phase-field models (either 2D or 3D) are necessary to validate this hypothesis of dual grain growth modes.

The high occurrence of twin boundaries in aluminum alloys is unexpected, given the high energy typically required to form twins within

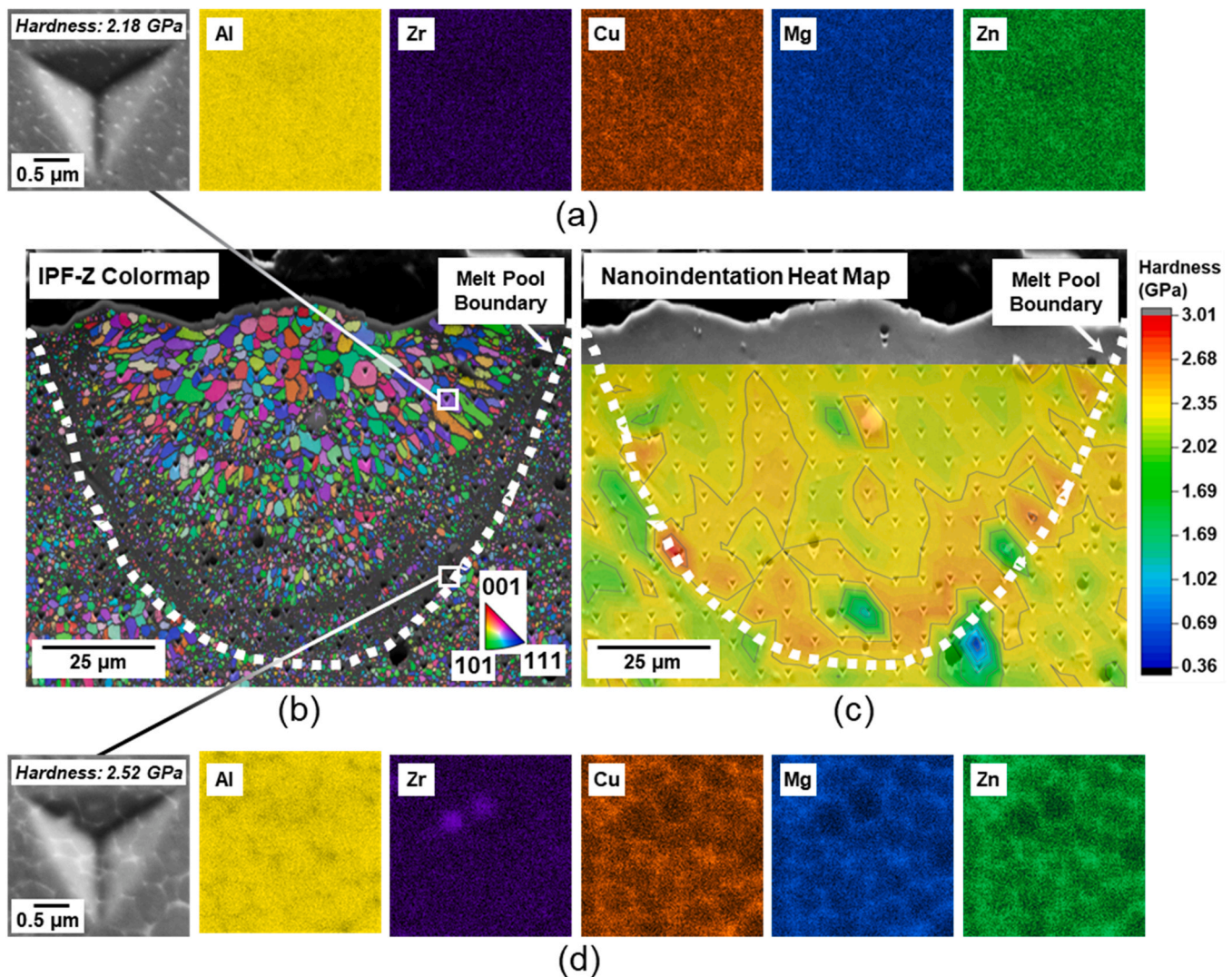


Fig. 10. (c) Nanoindentation heat map overlaid on SEM image an autogenous AA7A77 single pass and (d) corresponding IPF-Z color map. (a)(d) SEM images and EDS elemental maps showing characteristic indentations within the (d) fine and (a) coarse grain regions.

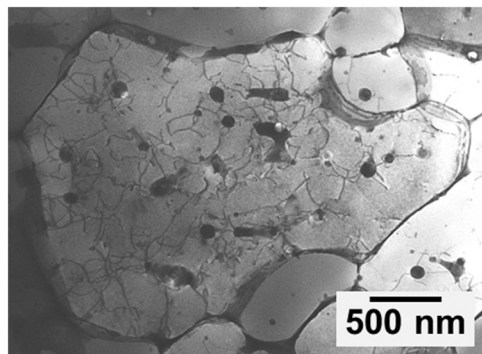


Fig. 11. Bright field TEM image showing dislocation networks around the interdendritic quasicrystals within the coarse aluminum grains in the AA7A77 microstructure.

FCC Al [70]. Specifically, the energy required to form a coherent twin in FCC Al is 0.119 J/m². In contrast, other FCC metals, such as gold require considerably less energy, nearly an order of magnitude lower at 0.015 J/m² [71]. Previous studies have attributed the unusually high occurrence of twin boundaries in cast [54] or AM [72,73] aluminum

alloys to icosahedral short-range order-enhanced nucleation [54,70,73, 74]. It has been postulated that this nucleation mechanism contributed to grain refinement of the aluminum matrix. Additionally, icosahedral short-range order of deeply undercooled liquids has been experimentally verified to form quasicrystals [75]. Within the AA7A77 system, icosahedral short-range order-enhanced nucleation is a provocative idea because these sites could not only promote nucleation of the aluminum matrix but also the icosahedral quasicrystals found within the microstructure. Although the high fractions of aluminum twin boundaries and icosahedral quasicrystals within the microstructure appeared to support the icosahedral short-range order-enhanced nucleation hypothesis, further work is needed to confirm whether this mechanism applies to AA7A77 and similar materials.

4.2. Formation of icosahedral quasicrystal and implications for enhanced properties

Although researchers have reported the presence of quasicrystals in the microstructure of AM aluminum alloys, a thorough analysis of their formation mechanism is lacking. Using our detailed experimental evidence in combination with computational thermodynamic simulations, the following formation mechanism is proposed and shown schematically in Fig. 12. During solidification, the final transition from liquid to

solid occurs within the interdendritic regions and along grain boundaries. Our observations, as shown in Fig. 6, clearly demonstrate that the quasicrystals formed at these locations within the AA7A77 microstructure. The spatial distribution and the morphological characteristics of these quasicrystalline phases strongly suggest that the formation of the quasicrystals occurred near the completion of the solidification process. As indicated by Scheil simulations, near the termination of solidification, a thermodynamic driving force exists at 95 % fraction of solid and a temperature of 496 °C to form the T-phase or $\text{Mg}_{32}(\text{Al}, \text{Zn}, \text{Cu})_{49}$, which has a body-centered cubic crystal structure and a lattice parameter between 1.428 nm and 1.435 nm [76–78]. The predicted composition of this crystalline T-phase is similar to our observed quasicrystal, as listed in Table 3.

The compositional similarities between the T-phase and our observed icosahedral quasicrystals may not be coincidental and strongly suggests the metastable nature of the quasicrystals. The formation of quasicrystals is known to be highly sensitive to the compositions that tend towards specific atomic ratios among the constituent elements to achieve long-range aperiodic ordering. However, the correct composition is merely a necessary condition, not a sufficient one, as the formation of the quasicrystals also depends on the processing conditions. For example, an Al–Zn–Mg–Cu alloy forms an icosahedral quasicrystal with a quasilattice constant of 0.515 nm under rapid solidification, at cooling rates ranging between 1×10^5 °C/s and 1×10^7 °C/s [59]. In contrast, no quasicrystals were observed in a similar Al–Zn–Mg–Cu alloy processed by conventional casting and heat treatment. Instead, the cubic T-phase, denoted as $\text{Mg}_{32}(\text{Al}, \text{Zn}, \text{Cu})_{49}$, was identified within the microstructures [79].

The hardness data demonstrate that the presence of the quasicrystals benefits the mechanical properties of the as-fabricated AA7A77. To exploit this behavior for applications, it is crucial to understand the transformation pathways and kinetics from the metastable icosahedral quasicrystals to a thermodynamically stable phase, likely the T-phase. T-phase is relevant because in addition to the compositional similarity, a structural similarity between T-phase and the icosahedral quasicrystals also exists, with previous reports suggesting the T-phase serves as the icosahedral quasicrystal's one-to-one cubic crystalline approximant [80]. Determining the conditions that facilitate such a phase transformation will allow us to evaluate the energy barrier that must be overcome and the long-term stability of these metastable quasicrystals.

We have demonstrated that with the bimodal microstructure and the formation of different metastable phases, the as-fabricated AA7A77 has a hardness comparable to that of the peak-aged 7075 alloy. The AA7A77 is also precipitation hardenable, creating a possibility to improve its

mechanical performance through subsequent heat treatment. Incorporating quasicrystals, known for their high hardness, into lightweight metals can also produce materials with high strength-to-weight ratios, enhanced wear resistance, and improved high-temperature mechanical properties [81–83]. These possibilities suggest a new research direction to engineer materials that utilize AM's rapid solidification to introduce quasicrystals into the material's microstructure, potentially developing novel high-performance alloys.

5. Conclusions

This study provides a comprehensive analysis of the microstructure and metastable phase formation in a commercially available AM aluminum alloy (AA7A77) in its as-fabricated condition. Through a multi-length scale characterization, a bimodal grain structure is observed, consisting of both fine equiaxed grains located near the melt-pool boundary and coarse elongated grains located in the center of the melt pool. This bimodal structure arises primarily from the solidification process rather than remelting/reheating from subsequent laser passes. Furthermore, the rapid solidification inherent to the AM process contributed to metastable phase formation. Specifically, two metastable phases were identified: a cuboidal phase, which formed at the onset of solidification and is localized within fine grains, and a $\text{Mg}_{32}(\text{Al}, \text{Zn}, \text{Cu})_{49}$ icosahedral quasicrystal, which developed at the final stages of solidification, predominantly within coarse grains and along grain boundaries. The results indicate the formation of these quasicrystals is influenced by two primary factors: (1) a thermodynamic driving force of a secondary phase conducive to quasicrystal formation and (2) the rapid cooling rates associated with AM. These metastable phases and microstructural features result in hardness levels comparable to those of the peak-aged AA7075. This promising result implies that the intentional incorporation of quasicrystals into the microstructure via AM could be advantageous for developing future high-performance materials.

The primary conclusions from this work are as follows:

- Within fine aluminum grains, metastable cuboidal $\text{L}_{12} \text{Al}_3\text{Zr}$ precipitates were identified at the grain centers. These precipitates have a similar lattice parameter to that of the matrix, and a cube-on-cube orientation relationship with the matrix, supporting the role of the Al_3Zr precipitate as an effective aluminum grain refiner.
- Quasicrystals were identified within the interdendritic regions of the coarse grains and along grain boundaries. Although the location and morphology of these quasicrystals were different, their composition and structure were identical. These quasicrystals were determined to

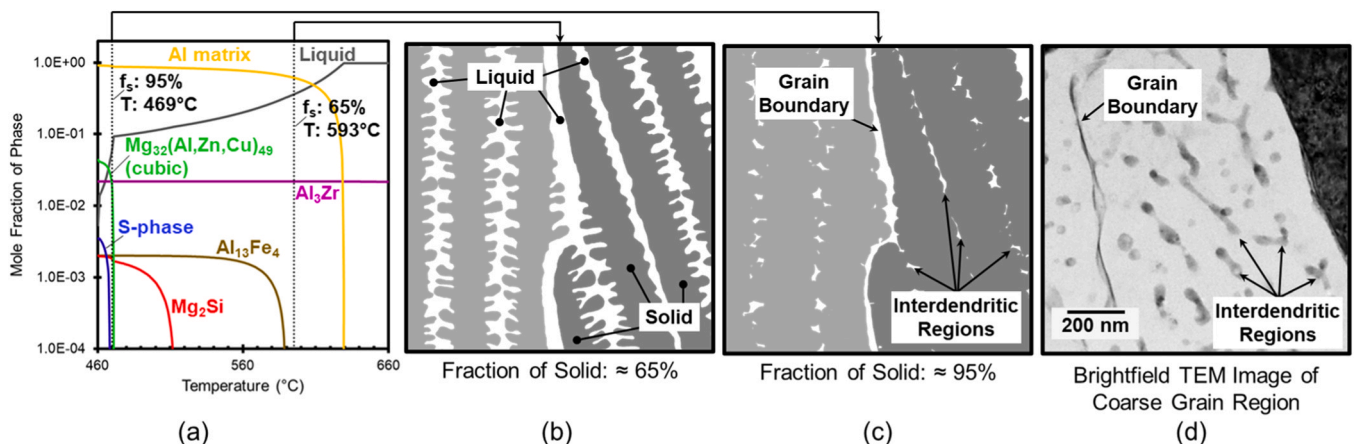


Fig. 12. (a) Predicted phase fraction as a function of temperature under Scheil conditions, showing the formation of cubic $\text{Mg}_{32}(\text{Al}, \text{Zn}, \text{Cu})_{49}$ near the termination of solidification. Schematic of the microstructural evolution (b) near the middle and (c) near termination of solidification. Near the termination of solidification, the last regions to solidify are along grain boundaries and within interdendritic regions, (d) which were also the locations where the metastable $\text{Mg}_{32}(\text{Al}, \text{Zn}, \text{Cu})_{49}$ icosahedral quasicrystal was observed within coarse grain regions.

be $\text{Mg}_{32}(\text{Al}, \text{Zn}, \text{Cu})_{49}$ icosahedral quasicrystals with a point group of $\bar{m}35$ and a quasilattice constant of $0.516 \text{ nm} \pm 0.001 \text{ nm}$.

- The location and morphology of the quasicrystal indicated their formation occurred near the end of solidification. This conclusion was corroborated through computational simulations, which revealed a secondary phase conducive to quasicrystal formation was predicted to form during the late stage of solidification.
- Nanoindentation data revealed a hardness of $2.34 \text{ GPa} \pm 0.15 \text{ GPa}$ for the as-fabricated AA7A77 material, comparable to the hardness of peak-aged. Spatially-resolved measurements showed that the hardness values for fine-grain and coarse-grain regions were $2.28 \text{ GPa} \pm 0.11 \text{ GPa}$ and $2.45 \text{ GPa} \pm 0.16 \text{ GPa}$, respectively. Extensive dislocation networks were observed around the quasicrystals within the coarse grains, contributing to the elevated hardness values.

Declaration of Competing Interest

The authors declare that they have no known competing financial interests or personal relationships that could have appeared to influence the work reported in this paper.

Acknowledgements

A.D. Iams would like to thank Ms. Maureen E. Williams for her support and guidance preparing TEM samples. Thanks to Joseph R. Michael for a critical review of the paper and helpful comments. A.D. Iams also acknowledges the late Professor Earle R. Ryba for the helpful discussions on the formation of quasicrystals. A.D. Iams acknowledges support from the U.S. Department of Commerce, National Institute of Standards and Technology under the financial assistance award 70NANB22H028. We acknowledge a NIST Cross-OU collaboration grant that funded this work.

Appendix A. Supporting information

Supplementary data associated with this article can be found in the online version at [doi:10.1016/j.jallcom.2025.180281](https://doi.org/10.1016/j.jallcom.2025.180281).

References

- [1] N.T. Aboulkhair, M. Simonelli, L. Parry, I. Ashcroft, C. Tuck, R. Hague, 3D printing of Aluminium alloys: additive manufacturing of aluminium alloys using selective laser melting, *Prog. Mater. Sci.* 106 (2019), <https://doi.org/10.1016/j.pmatsci.2019.100578>.
- [2] H.R. Kotadia, G. Gibbons, A. Das, P.D. Howes, A review of laser powder bed fusion additive manufacturing of aluminium alloys: microstructure and properties, *Addit. Manuf.* 46 (2021), <https://doi.org/10.1016/j.addma.2021.102155>.
- [3] S. Dixit, S. Liu, Laser additive manufacturing of high-strength aluminum alloys: challenges and strategies, *J. Manuf. Mater. Process.* 6 (2022), <https://doi.org/10.3390/jmmp6060156>.
- [4] P.A. Rometsch, Y. Zhu, X. Wu, A. Huang, Review of high-strength aluminium alloys for additive manufacturing by laser powder bed fusion, *Mater. Des.* 219 (2022), <https://doi.org/10.1016/j.matdes.2022.110779>.
- [5] R. Nadella, D.G. Eskin, Q. Du, L. Katgerman, Macrosegregation in direct-chill casting of aluminium alloys, *Prog. Mater. Sci.* 53 (2008) 421–480, <https://doi.org/10.1016/j.pmatsci.2007.10.001>.
- [6] Y. Li, H. Li, L. Katgerman, Q. Du, J. Zhang, L. Zhuang, Recent advances in hot tearing during casting of aluminium alloys, *Prog. Mater. Sci.* 117 (2021), <https://doi.org/10.1016/j.pmatsci.2020.100741>.
- [7] I. Zhironov, S. Mekhontsev, B. Lane, S. Grantham, N. Bura, Accurate determination of laser spot position during laser powder bed fusion process thermography, *Manuf. Lett.* 23 (2020) 49–52, <https://doi.org/10.1016/j.mfglet.2019.12.002>.
- [8] C. Brice, R. Shenoy, M. Kral, K. Buchannan, Precipitation behavior of aluminum alloy 2139 fabricated using additive manufacturing, *Mater. Sci. Eng. A* 648 (2015) 9–14, <https://doi.org/10.1016/j.msea.2015.08.088>.
- [9] A. Mauduit, S. Pillot, H. Gransac, Study of the suitability of aluminum alloys for additive manufacturing by laser powder bed fusion, *Bull. Ser. B* 79 (2017) 219–238.
- [10] W. Stopyra, K. Gruber, I. Smolina, T. Kurzynowski, B. Kuźnicka, Laser powder bed fusion of AA7075 alloy: influence of process parameters on porosity and hot cracking, *Addit. Manuf.* 35 (2020), <https://doi.org/10.1016/j.addma.2020.101270>.
- [11] L. Zhou, H. Hyer, S. Thapliyal, R.S. Mishra, B. McWilliams, K. Cho, Y. Sohn, Process-dependent composition, microstructure, and printability of Al-Zn-Mg and Al-Zn-Mg-Sc-Zr alloys manufactured by laser powder bed fusion, *Met. Mater. Trans. A Phys. Met. Mater. Sci.* 51 (2020) 3215–3227, <https://doi.org/10.1007/s11661-020-05768-3>.
- [12] N. Kaufmann, M. Imran, T.M. Wischeropp, C. Emmelmann, S. Siddique, F. Walther, Influence of process parameters on the quality of aluminium alloy EN AW 7075 using Selective Laser Melting (SLM), in: *Phys Procedia*, Elsevier B.V., 2016, pp. 918–926, <https://doi.org/10.1016/j.phpro.2016.08.096>.
- [13] J.H. Martin, B.D. Yahata, J.M. Hundley, J.A. Mayer, T.A. Schaedler, T.M. Pollock, 3D printing of high-strength aluminium alloys, *Nature* 549 (2017) 365–369, <https://doi.org/10.1038/nature23894>.
- [14] Z. Geng, C. Chen, M. Song, J. Luo, J. Chen, R. Li, K. Zhou, High strength Al_{0.7}CoCrFeNi_{2.4} hypereutectic high entropy alloy fabricated by laser powder bed fusion via triple-nanoprecipitation, *J. Mater. Sci. Technol.* 187 (2024) 141–155, <https://doi.org/10.1016/j.jmst.2023.11.054>.
- [15] S.K. Kairi, O. Gharbi, J. Nicklaus, D. Jiang, C.R. Hutchinson, N. Birbilis, On the characterization of a hitherto unreported icosahedral quasicrystal phase in additively manufactured aluminium alloy AA7075, *Met. Mater. Trans. A Phys. Met. Mater. Sci.* 50 (2019) 529–533, <https://doi.org/10.1007/s11661-018-5025-1>.
- [16] M.C. Brennan, J.S. Keist, T.A. Palmer, Defects in metal additive manufacturing processes, *J. Mater. Eng. Perform.* 30 (2021) 4808–4818, <https://doi.org/10.1007/s11665-021-05919-6>.
- [17] D. Koutny, D. Palousek, L. Pantelejev, C. Hoeller, R. Pichler, L. Tesicky, J. Kaiser, Influence of scanning strategies on processing of aluminium alloy EN AW 2618 using selective laser melting, *Materials* 11 (2018), <https://doi.org/10.3390/ma11020298>.
- [18] M.C.H. Karg, B. Ahuja, S. Wiesenmayer, S.V. Kuryntsev, M. Schmidt, Effects of process conditions on the mechanical behavior of aluminium wrought alloy EN AW-2219 (AlCu6Mn) additively manufactured by laser beam melting in powder bed, *Micromachines* (Basel) 8 (2017), <https://doi.org/10.3390/mi8010023>.
- [19] Y. Otani, Y. Kusaki, K. Itagaki, S. Sasaki, Microstructure and mechanical properties of A7075 alloy with additional Si objects fabricated by selective laser melting, *Mater. Trans.* 60 (2019) 2143–2150, <https://doi.org/10.2320/matertrans.Y-M2019837>.
- [20] Q. Tan, J. Zhang, Q. Sun, Z. Fan, G. Li, Y. Yin, Y. Liu, M.X. Zhang, Inoculation treatment of an additively manufactured 2024 aluminium alloy with titanium nanoparticles, *Acta Mater.* 196 (2020) 1–16, <https://doi.org/10.1016/j.actamat.2020.06.026>.
- [21] T. Qi, H. Zhu, H. Zhang, J. Yin, L. Ke, X. Zeng, Selective laser melting of Al7050 powder: melting mode transition and comparison of the characteristics between the keyhole and conduction mode, *Mater. Des.* 135 (2017) 257–266, <https://doi.org/10.1016/j.matdes.2017.09.014>.
- [22] Y. Otani, S. Sasaki, Effects of the addition of silicon to 7075 aluminum alloy on microstructure, mechanical properties, and selective laser melting processability, *Mater. Sci. Eng. A* 777 (2020), <https://doi.org/10.1016/j.msea.2020.139079>.
- [23] M. Kumar, G.J. Gibbons, A. Das, I. Manna, D. Tanner, H.R. Kotadia, Additive manufacturing of aluminium alloy 2024 by laser powder bed fusion: microstructural evolution, defects and mechanical properties, *Rapid Prototyp. J.* 27 (2021) 1388–1397, <https://doi.org/10.1108/RPJ-10-2020-0241>.
- [24] S. Kou, *Welding Metallurgy*, 3rd ed., Wiley, 2020.
- [25] Merton C. Flemings, *Solidification Processing*, 1974.
- [26] A.B. Spierings, K. Dawson, M. Voegtlin, F. Palm, P.J. Uggowitzer, Microstructure and mechanical properties of as-processed scandium-modified aluminium using selective laser melting, *CIRP Ann. Manuf. Technol.* 65 (2016) 213–216, <https://doi.org/10.1016/j.cirp.2016.04.057>.
- [27] A.B. Spierings, K. Dawson, T. Heeling, P.J. Uggowitzer, R. Schaublin, F. Palm, K. Wegener, Microstructural features of Sc- and Zr-modified Al-Mg alloys processed by selective laser melting, *Mater. Des.* 115 (2017) 52–63, <https://doi.org/10.1016/j.matdes.2016.11.040>.
- [28] J.R. Croteau, S. Griffiths, M.D. Rossell, C. Leinenbach, C. Kenel, V. Jansen, D. N. Seidman, D.C. Dunand, N.Q. Vo, Microstructure and mechanical properties of Al-Mg-Zr alloys processed by selective laser melting, *Acta Mater.* 153 (2018) 35–44, <https://doi.org/10.1016/j.actamat.2018.04.053>.
- [29] S. Griffiths, M.D. Rossell, J. Croteau, N.Q. Vo, D.C. Dunand, C. Leinenbach, Effect of laser rescanning on the grain microstructure of a selective laser melted Al-Mg-Zr alloy, *Mater. Charact.* 143 (2018) 34–42, <https://doi.org/10.1016/j.matchar.2018.03.033>.
- [30] H. Zhang, H. Zhu, X. Nie, J. Yin, Z. Hu, X. Zeng, Effect of Zirconium addition on crack, microstructure and mechanical behavior of selective laser melted Al-Cu-Mg alloy, *Scr. Mater.* 134 (2017) 6–10, <https://doi.org/10.1016/j.scriptamat.2017.02.036>.
- [31] T.C. Lin, C. Cao, M. Sokoluk, L. Jiang, X. Wang, J.M. Schoenung, E.J. Lavernia, X. Li, Aluminum with dispersed nanoparticles by laser additive manufacturing, *Nat. Commun.* 10 (2019), <https://doi.org/10.1038/s41467-019-12047-2>.
- [32] M. Opprecht, J.P. Garandet, G. Roux, C. Flament, M. Soulier, A solution to the hot cracking problem for aluminium alloys manufactured by laser beam melting, *Acta Mater.* 197 (2020) 40–53, <https://doi.org/10.1016/j.actamat.2020.07.015>.
- [33] S.Y. Zhou, Y. Su, H. Wang, J. Enz, T. Ebel, M. Yan, Selective laser melting additive manufacturing of 7xxx series Al-Zn-Mg-Cu alloy: cracking elimination by co-incorporation of Si and TiB₂, *Addit. Manuf.* 36 (2020), <https://doi.org/10.1016/j.addma.2020.101458>.
- [34] N. Qbau, N.D. Nam, N.X. Ca, N.T. Hien, The crack healing effect of scandium in aluminium alloys during laser additive manufacturing, *J. Manuf. Process* 50 (2020) 241–246, <https://doi.org/10.1016/j.jmapro.2019.12.050>.

- [35] L. Ren, H. Gu, W. Wang, S. Wang, C. Li, Z. Wang, Y. Zhai, P. Ma, Effect of Sc content on the microstructure and properties of Al–Mg–Sc alloys deposited by wire arc additive manufacturing, *Met. Mater. Int.* (2020), <https://doi.org/10.1007/s12540-020-00763-0>.
- [36] P. Mair, L. Kaserer, J. Braun, N. Weinberger, I. Letofsky-Papst, G. Leichtfried, Microstructure and mechanical properties of a TiB₂-modified Al–Cu alloy processed by laser powder-bed fusion, *Mater. Sci. Eng. A* 799 (2021), <https://doi.org/10.1016/j.msea.2020.140209>.
- [37] T. Fan, Z. Ruan, F. Zhong, C. Xie, X. Li, D. Chen, P. Tang, Y. Wu, Nucleation and growth of L1₂-Al₃RE particles in aluminum alloys: a first-principles study, *J. Rare Earths* 41 (2023) 1116–1126, <https://doi.org/10.1016/j.jre.2022.05.018>.
- [38] The Aluminum Association, Registration Record Series, Purple Sheets, Designations and Chemical Composition Limits for Aluminum Powders and Aluminum Alloy Powders, 2022. (www.aluminum.org).
- [39] Thermo-Calc Software, Thermo-Calc Version 2022b, n.d.
- [40] J.O. Andersson, T. Helander, L. Höglund, P.F. Shi, B. Sundman, Thermo-Calc and DICTRA, Computational Tools for Materials Science, *CALPHAD* 26 (2002) 273–312.
- [41] Thermo-Calc Software, TCAL/Al-Alloys Database Version 3, n.d.
- [42] E. Scheil, Bemerkungen zur schichtkristallbildung, *Int. J. Mater. Res.* 34 (1942) 70–72.
- [43] G.H. Gulliver, The quantitative effect of rapid cooling upon the constitution of binary alloys, *J. Inst. Met.* 13 (1915) 263.
- [44] B. Bocklund, L.D. Bobbio, R.A. Otis, A.M. Beese, Z.K. Liu, Experimental validation of Scheil–Gulliver simulations for gradient path planning in additively manufactured functionally graded materials, *Materialia* (Oxf.) 11 (2020), <https://doi.org/10.1016/j.mtl.2020.100689>.
- [45] G. Cliff, G.W. Lorimer, The quantitative analysis of thin specimens, *J. Microsc.* 103 (1975) 203–207, <https://doi.org/10.1111/j.1365-2818.1975.tb03895.x>.
- [46] W.C. Oliver, G.M. Pharr, Measurement of hardness and elastic modulus by instrumented indentation: advances in understanding and refinements to methodology, *J. Mater. Res.* 19 (2004) 3–20. (www.mrs.org/publications/jmr/poly.html).
- [47] John E. Hatch, *Aluminum: Properties and Physical Metallurgy*, 1984.
- [48] T. DebRoy, H.L. Wei, J.S. Zuback, T. Mukherjee, J.W. Elmer, J.O. Milewski, A. M. Beese, A. Wilson-Heid, A. De, W. Zhang, Additive manufacturing of metallic components – process, structure and properties, *Prog. Mater. Sci.* 92 (2018) 112–224, <https://doi.org/10.1016/j.pmatsci.2017.10.001>.
- [49] J.H. Martin, B. Yahata, J. Mayer, R. Mone, E. Stonkevitch, J. Miller, M.R. O'Masta, T. Schaedler, J. Hundley, P. Callahan, T. Pollock, Grain refinement mechanisms in additively manufactured nano-functionalized aluminum, *Acta Mater.* 200 (2020) 1022–1037, <https://doi.org/10.1016/j.actamat.2020.09.043>.
- [50] S.S.T.A. Hori, S. Metastable phase and grain refinement in rapidly solidified Al–Zr alloys, *J. Jpn. Inst. Light Met.* 31 (1981) 793–797.
- [51] R. Ichikawa, T. Ohashi, T. Ikeda, Effects of cooling rate and supercooling degree on solidified structure of Al–Mn, Al–Cr and Al–Zr in rapid solidification, *Trans. Jpn. Inst. Met.* 12 (1971) 280–284.
- [52] T. Ohashi, R. Ichikawa, Grain refinement in aluminium–zirconium and aluminium–titanium alloys by metastable phases, *Zeitschrift fuer Metallkunde* 64 (1973) 517–521.
- [53] K.E. Knippling, D.C. Dunand, D.N. Seidman, Nucleation and precipitation strengthening in dilute Al–Ti and Al–Zr alloys, *Met. Mater. Trans. A Phys. Met. Mater. Sci.* 38 (2007) 2552–2563, <https://doi.org/10.1007/s11661-007-9283-6>.
- [54] G. Kurtuldu, P. Jarry, M. Rappaz, Influence of Cr on the nucleation of primary Al and formation of twinned dendrites in Al–Zn–Cr alloys: can icosahedral solid clusters play a role? *Acta Mater.* 61 (2013) 7098–7108, <https://doi.org/10.1016/j.actamat.2013.07.056>.
- [55] B.L. Bramfitt, The effect of carbide and nitride additions on the heterogeneous nucleation behavior of liquid iron, *Metall. Trans.* 1 (1970) 1987–1995.
- [56] J.Q. Guo, K. Ohtera, An intermediate phase appearing in L1₂-Al₃Zr to D0₂₃-Al₃Zr phase transformation of rapidly solidified Al–Zr alloys, *Mater. Lett.* 27 (1996) 343–347.
- [57] D. Shechtman, J.L. Hutchison, L.H. Robins, E.N. Farahaugh, A. Feldman, Growth defects in diamond films, *J. Mater. Res.* 8 (1993) 473–479, <https://doi.org/10.1557/JMR.1993.0473>.
- [58] J.W. Cahn, D. Shechtman, D. Gratias, Indexing of icosahedral quasicrystalline crystals, *J. Mater. Res.* 1 (1986) 13–26, <https://doi.org/10.1557/JMR.1986.0013>.
- [59] N. Mukhopadhyay, G. Subbanna, S. Ranganathan, K. Chattopadhyay, An electron microscopic study of quasicrystals in a quaternary alloy: Mg₃₂ (Al, Zn, Cu)₄₉, *Scr. Metall.* 20 (1986) 525–528.
- [60] V. Elser, Indexing problems in quasicrystal diffraction, *Phys. Rev. B* 32 (1985) 4892–4898, <https://doi.org/10.1103/PhysRevB.32.4892>.
- [61] S. Wu, Z. Lei, B. Li, J. Liang, Y. Chen, Hot cracking evolution and formation mechanism in 2195 Al–Li alloy printed by laser powder bed fusion, *Addit. Manuf.* 54 (2022), <https://doi.org/10.1016/j.addma.2022.102762>.
- [62] M. Wang, R. Li, T. Yuan, J. Kang, P. Niu, D. Zheng, Z. Fan, The evolution of quasicrystal during additive manufacturing and aging treatment of a Si-modified Al–Mn–Sc alloy, *Mater. Sci. Eng. A* 859 (2022), <https://doi.org/10.1016/j.msea.2022.144206>.
- [63] A.P. Babu, S.K. Kairay, A. Huang, N. Birbilis, Laser powder bed fusion of high solute Al–Zn–Mg alloys: processing, characterisation and properties, *Mater. Des.* 196 (2020), <https://doi.org/10.1016/j.matdes.2020.109183>.
- [64] J. Bi, Z. Lei, Y. Chen, X. Chen, Z. Tian, J. Liang, X. Zhang, X. Qin, Microstructure and mechanical properties of a novel Sc and Zr modified 7075 aluminum alloy prepared by selective laser melting, *Mater. Sci. Eng.: A* 768 (2019), <https://doi.org/10.1016/j.msea.2019.138478>.
- [65] S.S. Singh, C. Schwartzstein, J.J. Williams, X. Xiao, F. De Carlo, N. Chawla, 3D microstructural characterization and mechanical properties of constituent particles in Al 7075 alloys using X-ray synchrotron tomography and nanoindentation, *J. Alloy. Compd.* 602 (2014) 163–174, <https://doi.org/10.1016/j.jallcom.2014.03.010>.
- [66] J.P. Best, X. Maeder, J. Michler, A.B. Spierings, Mechanical anisotropy investigated in the complex SLM-processed Sc- and Zr-modified Al–Mg alloy microstructure, *Adv. Eng. Mater.* 21 (2019), <https://doi.org/10.1002/adem.201801113>.
- [67] A. Dhal, S. Thapliyal, S. Gaddam, P. Agrawal, R.S. Mishra, Multiscale hierarchical and heterogeneous mechanical response of additively manufactured novel Al alloy investigated by high-resolution nanoindentation mapping, *Sci. Rep.* 12 (2022), <https://doi.org/10.1038/s41598-022-23083-2>.
- [68] K. Stan-Glowinska, A. Zieba, L. Rogal, Characterization of quasicrystalline precipitates in artificially aged Al–Mg–Zn alloy with Ga addition, *J. Mater. Res. Technol.* 21 (2022) 1749–1759, <https://doi.org/10.1016/j.jmrt.2022.10.020>.
- [69] Y. Gu, L. Chen, Switching of controlling mechanisms during the rapid solidification of a melt pool in additive manufacturing, *ArXiv:2208.01487* (2022).
- [70] M. Rappaz, P. Jarry, G. Kurtuldu, J. Zollinger, Solidification of metallic alloys: does the structure of the liquid matter? *Met. Mater. Trans. A Phys. Met. Mater. Sci.* 51 (2020) 2651–2664, <https://doi.org/10.1007/s11661-020-05770-9>.
- [71] S. Ino, Stability of multiply-twinned particles, *J. Phys. Soc. Jpn.* 27 (1969) 941–953.
- [72] C. Galera-Rueda, M.L. Montero-Sistiaga, K. Vanmeensel, M. Godino-Martínez, J. Llorca, M.T. Pérez-Prado, Icosahedral quasicrystal-enhanced nucleation in Al alloys fabricated by selective laser melting, *Addit. Manuf.* 44 (2021), <https://doi.org/10.1016/j.addma.2021.102053>.
- [73] M. Buttard, G. Martin, X. Bataillon, G. Renou, P. Lhuissier, J. Villanova, B. Chehab, P. Jarry, J.-J. Blandin, P. Donnadieu, Towards an alloy design strategy by tuning liquid local ordering: what solidification of an Al-alloy designed for laser powder bed fusion teaches us, *Addit. Manuf.* 61 (2023) 103313, <https://doi.org/10.1016/j.addma.2022.103313>.
- [74] C. Galera-Rueda, M.L. Montero-Sistiaga, K. Vanmeensel, M. Godino-Martínez, J. Llorca, M.T. Pérez-Prado, Icosahedral quasicrystal-enhanced nucleation in Al alloys fabricated by selective laser melting, *Addit. Manuf.* 44 (2021), <https://doi.org/10.1016/j.addma.2021.102053>.
- [75] D. Holland-Moritz, T. Schenk, V. Simonet, R. Bellissent, P. Convert, T. Hansen, Short-range order in undercooled melts forming quasicrystals and approximants, 2002. (www.elsevier.com/locate/jallcom).
- [76] G. Bergman, J. Waugh, L. Pauling, Crystal structure of the intermetallic compound Mg₃₂ (Al, Zn)₄₉ and related phases, *Nature* 169 (1952) 1057–1058.
- [77] G. Bergman, J. Waugh, L. Pauling, The crystal structure of the metallic phase Mg₃₂ (Al, Zn)₄₉, *Acta Crystallogr.* 10 (1957) 254–259.
- [78] J.H. Auld, B.E. Williams, X-ray powder data of T phases composed of aluminum and magnesium with silver, copper or zinc, *Acta Crystallogr.* 21 (1966) 830–831.
- [79] L.L. Rokhlin, T.V. Dobatkina, N.R. Bocharov, E.V. Lysova, Investigation of phase equilibria in alloys of the Al–Zn–Mg–Cu–Zr–Sc system, *J. Alloy. Compd.* (2004) 10–16, <https://doi.org/10.1016/j.jallcom.2003.08.003>.
- [80] D.P. Shoemaker, C.B. Shoemaker, Icosahedral Coordination in Metallic Crystals, in: *Introduction to Quasicrystals: Aperiodicity and Order*, 1988: pp. 1–57. <https://doi.org/10.1016/b978-0-12-040601-2.50006-8>.
- [81] W. Wolf, C. Bolfarini, C.S. Kiminami, W.J. Botta, Fabrication of Al-matrix composite reinforced with quasicrystals using conventional metallurgical fabrication methods, *Scr. Mater.* 173 (2019) 21–25, <https://doi.org/10.1016/j.scriptamat.2019.07.044>.
- [82] W. Wolf, L.P. Luiz, G. Zepon, C.S. Kiminami, C. Bolfarini, W.J. Botta, Single step fabrication by spray forming of large volume Al-based composites reinforced with quasicrystals, *Scr. Mater.* 181 (2020) 86–91, <https://doi.org/10.1016/j.scriptamat.2020.02.018>.
- [83] A.P.M. de Araujo, C.S. Kiminami, V. Uhlenwinkel, P. Gargarella, High-temperature tensile properties of an aluminum quasicrystal-forming alloy manufactured by laser powder bed fusion, *Mater. Sci. Eng.: A* 886 (2023), <https://doi.org/10.1016/j.msea.2023.145670>.